

Double Quantum Magnetometry at Large Static Magnetic Fields

C. Munuera-Javaloy,¹ I. Arrazola,¹ E. Solano,^{1,2,3} and J. Casanova^{1,2}

¹*Department of Physical Chemistry, University of the Basque Country UPV/EHU, Apartado 644, 48080 Bilbao, Spain*

²*IKERBASQUE, Basque Foundation for Science, Maria Diaz de Haro 3, 48013 Bilbao, Spain*

³*International Center of Quantum Artificial Intelligence for Science and Technology (QuArtist) and Department of Physics, Shanghai University, 200444 Shanghai, China*

We present a protocol to achieve double quantum magnetometry at large static magnetic fields. This is a regime where sensitive sample parameters, such as the chemical shift, get enhanced facilitating their characterization. In particular, our method delivers two-tone stroboscopic radiation patterns with modulated Rabi frequencies to achieve larger spectral signals. Furthermore, it does not introduce inhomogeneous broadening in the sample spectrum preventing signal misinterpretation. Moreover, our protocol is designed to work under realistic conditions such as the presence of moderate microwave power and errors on the radiation fields. Albeit we particularise to nitrogen vacancy centers, our protocol is general, thus applicable to distinct quantum sensors.

I. INTRODUCTION

The detection of magnetic signals emitted by spin ensembles is central in nanoscale nuclear magnetic resonance (nanoscale NMR)¹. Here, the hyperfine quantum state of a sensor such as the nitrogen vacancy (NV) center in diamond^{2,3} gets modified owing to the interaction with a nuclear or electronic target, leading to quantum sensing or quantum detection^{4,6}. To this end, the NV center quantum state is initialised and measured with a laser field, while it can be readily controlled with microwave (MW) radiation^{2,3}. In addition, the NV center presents quantum coherence, as well as a long decay time of the order of milliseconds, even at room temperature⁵. These are capacities that make NV centers in diamond ideal candidates for experiments at physiological conditions⁶. The coupling of the NV center with a target signal is typically conducted through dynamical decoupling (DD) techniques⁷ that, in addition, are able to remove noisy contributions over the sensor. Typically, continuous and pulsed (or stroboscopic) DD techniques are considered. The former relies on the Hartmann-Hahn resonance condition⁸, while certain stroboscopic DD radiation patterns, as those of the XY family^{9–15}, offer a superior level of robustness against errors on the control fields. First experiments with NV centers were able to detect classical electromagnetic fields¹⁶, while individual ¹³C nuclear spin emitters embedded in the diamond lattice have been identified with unprecedented resolution^{17–24}. In addition, nanoscale NMR of small volume samples of the order of picolitres, as well as of single molecules located external to the diamond lattice, have been achieved with single NV centers^{25–30} and with NV ensembles^{31,32}.

Several developments have been carried out to overcome the poor spectral resolution achievable with NV quantum sensors at room temperature. Among them, we have the combination of NV-based quantum detection with the presence of a quantum memory³³, or by synchronising NV measurements with a classical clock^{32,34,35}. These hybrid techniques have allowed the detection of coherent target signals with a frequency resolution of the order of few hertz with NV centers. Here, it is important to remark that, for all these applications the achievement of an NV-target coupling remains as the key ingredient, and the use of double quantum magnetome-

try (DQM) schemes^{36–38} permits enhanced signal acquisition. Furthermore, DQM techniques do not introduce a magnetic field gradient on the studied sample, which avoids inhomogeneous broadening in the measured spectrum³². Especially interesting for nanoscale NMR is the regime of large static magnetic fields^{30,39–41}. In these conditions, a large chemical shift is present³⁰. Note this is an important quantity that encodes structural information of the target sample such as the presence of different chemical bonds⁴². Furthermore, at large static magnetic fields the relaxation time of sensor gets enhanced⁴³, which provides with better frequency selectivity of the nuclear target³³. Consequently, having DQM schemes ready to be displayed at large static magnetic fields is of clear relevance in nanoscale NMR.

In this article, we provide DQM schemes able to conduct sensor-target coupling at large static magnetic fields. In addition, control errors over the sensor get removed owing to the intrinsic DD behaviour carried by our method. Via the use of two-tone stroboscopic MW radiation with modulated field amplitudes, we demonstrate the achievement of enhanced sensor-signal interaction with moderate power in the MW drivings. More importantly, our method removes inhomogeneous broadenings over the sample avoiding misinterpretation in the obtained spectrum. Hence, this is an optimal scheme for detecting natural deviations in the resonance frequencies of the target sample, such as those originated from chemical shifts. Our protocol is general, i.e., it can be displayed over different quantum sensors such as NV centers and silicon vacancy centers, while it can be adapted to any stroboscopic DD sequence used in nanoscale NMR.

II. THE METHOD

The Hamiltonian of an NV center in diamond under a MW driving $\sqrt{2}B_d^x \cos(\omega_{\text{MW}}t + \varphi)$ reads

$$H = DS_z^2 + |\gamma_e|B_z S_z + \sqrt{2}\gamma_e B_d^x \cos(\omega_{\text{MW}}t + \varphi)S_x. \quad (1)$$

Here $D = (2\pi) \times 2.87$ GHz is the zero field splitting, $|\gamma_e| = (2\pi) \times 28.024$ GHz/T, B_z is the static magnetic field aligned with the NV axis, while ω_{MW} and φ are the MW frequency and phase respectively. The spin-1 operators in Eq. (1) are $S_z =$

$|1\rangle\langle 1| - | -1\rangle\langle -1|$, and $S_x = \frac{1}{\sqrt{2}}(|1\rangle\langle 0| + |0\rangle\langle 1| + | -1\rangle\langle 0| + |0\rangle\langle -1|)$. The driving term $\sqrt{2}\gamma_e B_d^x \cos(\omega_{\text{MW}}t + \varphi)S_x$ in Eq. (1) leads to rotations in the NV hyperfine spin states, while an inspection to the S_x operator indicates that the MW driving does not generate transitions between the $|1\rangle$ and $| -1\rangle$.

For DQM we aim to induce rotations between the $|1\rangle$ and $| -1\rangle$ states by, e.g., a three-pulse-sequence involving the $|0\rangle$ state. In particular, in a rotating frame with respect to (w.r.t.) $DS_z^2 + |\gamma_e|B_z S_z$, Hamiltonian (1) is

$$H = \frac{\Omega(t)}{2}(e^{-i\varphi}|\pm 1\rangle\langle 0| + e^{i\varphi}|0\rangle\langle \pm 1|), \quad (2)$$

where the Rabi frequency $\Omega(t) = \gamma_e B_d^x(t)$, and the presence of $|\pm 1\rangle$ is selected by tuning $\omega_{\text{MW}} = D \pm |\gamma_e|B_z$ respectively. We denote the propagator (in the following we call it pulse) associated to Hamiltonian (2) as

$$U_{[2\phi_f, \varphi]}^{\pm 1}(t) = \exp\left[-i\phi(t)(e^{-i\varphi}|\pm 1\rangle\langle 0| + e^{i\varphi}|0\rangle\langle \pm 1|)\right], \quad (3)$$

where $\phi(t) = \int_{t_0}^t \frac{\Omega(s)}{2} ds$ with $t > t_0$, and ϕ_f is the final achieved phase after the application of the MW driving. Then, the three-pulse-sequence $\tilde{U}_{[\pi, 0]}^{[+1, -1, +1]} = U_{[\pi, 0]}^{+1} U_{[\pi, 0]}^{-1} U_{[\pi, 0]}^{+1}$ is equivalent to an effective π pulse on the S_z operator. This is

$$\left(\tilde{U}_{[\pi, 0]}^{[+1, -1, +1]}\right)^\dagger S_z \tilde{U}_{[\pi, 0]}^{[+1, -1, +1]} = -S_z. \quad (4)$$

Note that the previous result persists if one uses the alternative $\tilde{U}_{[\pi, \pi/2]}^{[-1, +1, -1]}$ three-pulse-sequence. See Supplemental Material⁴⁴ for an explanation of the three-pulse-sequence effect on the $S=1$ spin manifold¹ of the NV.

When a nuclear spin cluster is introduced in the formalism, Eq. (1) is completed to

$$H = DS_z^2 + |\gamma_e|B_z S_z + \sqrt{2}\gamma_e B_d^x \cos(\omega_{\text{MW}}t + \varphi)S_x - \sum_j \gamma_n B_z I_j^z + S_z \sum_j \vec{A}_j \cdot \vec{I}_j. \quad (5)$$

Here, γ_n is the nuclear gyromagnetic ratio, and \vec{A}_j is the hyperfine vector that mediates the interaction between an NV and the j th nucleus⁴⁶. In a rotating frame w.r.t. $DS_z^2 + |\gamma_e|B_z S_z$, Hamiltonian (5) reads

$$H = - \sum_j \gamma_n B_z I_j^z + S_z \sum_j \vec{A}_j \cdot \vec{I}_j + \frac{\Omega(t)}{2}(e^{-i\varphi}|\pm 1\rangle\langle 0| + e^{i\varphi}|0\rangle\langle \pm 1|). \quad (6)$$

We want to remark that we will use this Hamiltonian as the starting point for the following numerical simulations without doing any further assumption.

Typically, an NV spin qubit is selected between the $|0\rangle$ and one of the $|\pm 1\rangle$ hyperfine states. This is achieved via the next transformation (note we take $|0\rangle$ and $| +1\rangle$ as the NV qubit

states)

$$\begin{aligned} S_z \sum_j \vec{A}_j \cdot \vec{I}_j &= \left(|1\rangle\langle 1| - | -1\rangle\langle -1|\right) \sum_j \vec{A}_j \cdot \vec{I}_j \\ &= \frac{|1\rangle\langle 1| - |0\rangle\langle 0|}{2} + \frac{|1\rangle\langle 1| + |0\rangle\langle 0|}{2} \sum_j \vec{A}_j \cdot \vec{I}_j \\ &\quad - | -1\rangle\langle -1| \sum_j \vec{A}_j \cdot \vec{I}_j. \end{aligned} \quad (7)$$

Then, if the MW driving in Eq. (2) does not induce transitions to $| -1\rangle$ and the initial NV quantum state does not have a $| -1\rangle$ component, the last line in Eq. (7) can be safely removed. Consequently, one can establish the equivalence

$$S_z \sum_j \vec{A}_j \cdot \vec{I}_j \equiv \frac{\sigma_z}{2} \sum_j \vec{A}_j \cdot \vec{I}_j + \frac{I}{2} \sum_j \vec{A}_j \cdot \vec{I}_j, \quad (8)$$

with $\sigma_z = |1\rangle\langle 1| - |0\rangle\langle 0|$, and $I = |1\rangle\langle 1| + |0\rangle\langle 0|$. On the one hand, this approach known as single quantum magnetometry (SQM) presents the advantage of having easily implementable π pulses owing to the presence of a direct transition between the NV qubit states $|0\rangle$ and $|1\rangle$. On the other hand, the NV-nuclei coupling is reduced by a factor of 2, see first term at the right hand side of Eq. (8). From a different perspective, in SQM protocols the NV induced magnetic field gradient ($\frac{1}{2} \sum_j \vec{A}_j \cdot \vec{I}_j$) is useful to individually control ^{13}C spins in the diamond lattice²⁴ for, e.g., the implementation of quantum algorithms^{33,47}. However, as we will demonstrate later, the term ($\frac{1}{2} \sum_j \vec{A}_j \cdot \vec{I}_j$) introduces an inhomogeneous broadening leading to misinterpretation in the obtained NMR spectrum. This seriously affects to the determination of important structural parameters such as the chemical shift.

We deal with the main disadvantage of DQM schemes (i.e. the absence of a direct transition between $|1\rangle$ and $| -1\rangle$) with the three-pulse-sequences $\tilde{U}_{[\pi, 0]}^{[+1, -1, +1]}$ and $\tilde{U}_{[\pi, \pi/2]}^{[-1, +1, -1]}$. Nevertheless, we find that the performance of DQM schemes at the optimal situation of large B_z gets challenging. In particular, when a set of π pulses is applied on the S_z operator, Hamiltonian (6) (in a rotating frame w.r.t. the nuclear spin energy $-\sum_j \gamma_n B_z I_j^z$ and to the MW driving $\frac{\Omega(t)}{2}(e^{-i\varphi}|\pm 1\rangle\langle 0| + e^{i\varphi}|0\rangle\langle \pm 1|)$) reads

$$H = F(t) S_z \sum_j \left[A_j^x I_j^x \cos(\omega_L t) + A_j^y I_j^y \sin(\omega_L t) + A_j^z I_j^z \right]. \quad (9)$$

Here, the Larmor frequency $\omega_L = \gamma_n B_z$, and the NV-nuclei coupling constants are $A_j^{x,y} = |\vec{A}_j^{x,y}|$ where $\vec{A}_j^x = \vec{A}_j - (\vec{A}_j \cdot \hat{z}) \hat{z}$, $\vec{A}_j^y = \hat{z} \times \vec{A}_j$, and $I_j^x = \vec{I}_j \cdot \hat{x}_j$, $I_j^y = \vec{I}_j \cdot \hat{y}_j$ with $\hat{x}_j = \vec{A}_j^x / A_j^x$ and $\hat{y}_j = \vec{A}_j^y / A_j^y$. If we introduce a sequence of π pulses ordered in an even manner, $F(t)$ can be written as a sum of even harmonic functions as $F(t) = \sum_k f_k \cos(k\omega_D t)$. Here $\omega_D = \frac{2\pi}{T}$ with T being the elemental period of the sequence, see Fig. 1 (a), and the Fourier coefficients $f_k = 2/T \int_0^T F(s) \cos(k\omega_D s) ds$. Now, under the resonance condition (for the l th harmonic)

$$l\omega_D = \omega_L, \quad (10)$$

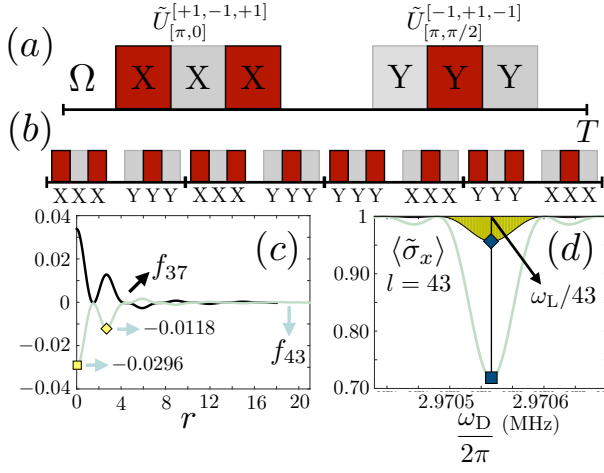


FIG. 1. (a) Top-hat Ω leading to $\tilde{U}_{[\pi,0]}^{[+1,-1,+1]}$ and $\tilde{U}_{[\pi,\pi/2]}^{[-1,+1,-1]}$. (b) Pulse structure of the sequence we repeat in our numerical simulations. (c) $f_{37,43}(r)$ (dark and clear curves, respectively). Yellow square and diamond marked the values of $f_{43}(r)$ we use in the next figure. (d) Computed signal for instantaneous π pulses (clear green curve) and for finite-width pulses (curve over dark-green area). Blue square and diamond mark the theoretically expected signal.

one finds the resonant NV-nuclei coupling Hamiltonian

$$H = \frac{f_l}{2} S_z \sum_j A_j^x I_j^x, \quad (11)$$

which reveals that the interaction strength of the NV with the nuclei depends on the value of f_l . For sequences with equally spaced instantaneous π pulses, one can calculate that $f_l = (-1)^{\frac{l-1}{2}} \frac{4}{\pi l}$. However, at large B_z the assumption of instantaneous pulses imply the transfer of a large amount of power to the sample. More specifically, in the typical case of top-hat π pulses (i.e. pulses generated with $H = \frac{\Omega}{2}(e^{-i\varphi}|\pm 1\rangle\langle 0| + e^{i\varphi}|0\rangle\langle \pm 1|)$ where the Rabi frequency Ω is constant) it is needed $\Omega \gg \omega_L$ to assure the instantaneous character of the π pulses (note that at $B_z = 3 \text{ T}^{30}$ the Larmor frequency is $\omega_L \approx (2\pi) \times 127 \text{ MHz}$). This is because the π pulse time is $t_\pi = \frac{\pi}{\Omega}$, then the condition $\frac{1}{2\Omega} \ll \frac{1}{\omega_L}$ must hold to certify that Hamiltonian (9) does not induce any evolution in the system during the π pulse duration. A failure of this condition is adverse for the NV nuclei coupling, since the f_l coefficient rapidly drops to zero. More specifically, one can calculate that, for odd k , and top-hat π pulses

$$f_l(r) = \frac{(-1)^{\frac{l-1}{2}} 36 \cos^3(\pi r)}{\pi l(-9 + 36r^2)}, \quad (12)$$

where r determines the relation of t_π with the nuclear Larmor period $\frac{2\pi}{\omega_L}$ through $t_\pi = \frac{2\pi r}{\omega_L}$, see⁴⁴. Equation (12) predicts a decay $\sim \frac{1}{r^2}$, while in the limit $r \rightarrow 0$ we recover the situation with instantaneous pulses, i.e. $f_l = (-1)^{\frac{l-1}{2}} \frac{4}{\pi l}$. In addition, one can find that $f_l = 0$ for even l . Finally, we point out that the issue of the decreasing f_l was previously shown in SQM³⁹ while here we observe it persists for DQM schemes.

In Fig. 1 (a) there is a scheme of the top-hat pulses leading to the three-pulse-sequences $\tilde{U}_{[\pi,0]}^{[+1,-1,+1]}$ and $\tilde{U}_{[\pi,\pi/2]}^{[-1,+1,-1]}$. In particular, dark-red pulses imply a π pulse between $|0\rangle$ and $|1\rangle$, while clear-grey between $|0\rangle$ and $|-1\rangle$. Furthermore, an X (Y) pulse corresponds to select $\varphi = 0$ ($\pi/2$) in Eq. (2). In Fig. 1 (b) we sketch the pulse sequence we will use in our numerical simulations for our DQM schemes. In Fig. 1 (c) we show the value of $f_l(r)$ (for $l = 37$ and 43). We observe that $f_{37,43}(r)$ decreases with r , leading to weaker values of the effective NV-nuclei coupling. This effect is confirmed in Fig. 1 (d) where we simulate Eq. (6) and compute the signal $\langle \tilde{\sigma}_x \rangle$ (with $\tilde{\sigma}_x = |1\rangle\langle -1| + |-1\rangle\langle 1|$) for different values of ω_D . For the sake of simplicity, we consider one NV and a single H nucleus such that the hyperfine vector is $\vec{A} = (2\pi) \times [7.39, 29.90, -4.61]$ kHz. Firstly, we simulate a situation with instantaneous pulses (clear-green curve) in an interval of ω_D that includes the resonance condition $43\omega_D = \omega_L$. In this latter case (i.e. on resonance) the NV-nucleus dynamics is governed by the Hamiltonian $H = \frac{f_{43}}{2} S_z A^x I^x$ with $f_{43} = -\frac{4}{43\pi} = -0.0296$, see Eq. (11). Note this is the value of f_{43} that corresponds to instantaneous π pulses, and it is marked in Fig. 1 (c) with a yellow square. The clear-green curve appears after repeating 200 times the sequence in Fig. 1 (b), which implies the delivery of 4600 π pulses on the $|0\rangle \leftrightarrow |\pm 1\rangle$ NV spin states (final sequence time is $\approx 0.194 \text{ ms}$). The curve over the dark-green area has been computed by applying finite-width top-hat π pulses such that $t_\pi \approx 7 \text{ ns}$. This implies π pulses generated with $\Omega \approx (2\pi) \times 71 \text{ MHz}$. The associated $f_{31} \approx -0.0158$ coefficient is marked in Fig. 1 (c) with a yellow diamond. In Fig. 1 (d) we compare the numerically obtained signal with the expected theoretical results according to the formula $\langle \tilde{\sigma}_x \rangle = \cos(\frac{f_{43}}{2} A^x t_f)$, see⁴⁴. The blue square is the signal associated to $f_{43} = -0.0296$ (instantaneous pulses) and blue diamond to $f_{43} = -0.0118$ (finite-width pulses). It can be observed a clear convergence between numerics and the theoretically expected signal, which confirms the presence of a severe signal reduction with realistic finite-width pulses.

III. DEMONSTRATION OF THE METHOD

To overcome this serious problem that limits the applicability of DQM schemes at the important regime of large B_z , we introduce a tailored Rabi frequency $\Omega(t)$ to generate the three-pulse-sequences $\tilde{U}_{[\pi,0]}^{[+1,-1,+1]}$ and $\tilde{U}_{[\pi,\pi/2]}^{[-1,+1,-1]}$. In this manner we will recover the value $f_l = (-1)^{\frac{l-1}{2}} \frac{4}{\pi l}$ corresponding to instantaneous pulses, with realistic finite-width π pulses that extends over several Larmor periods. In addition, and as we show in the next figure, these extended π pulses can be generated with only moderate MW power. At this point we want to comment that there are different manners of designing $\Omega(t)$, while we select the one described in the Supplemental Material⁴⁴.

In Fig. 2 we compare the signals (for a better comparison we plot $1 - \langle \tilde{\sigma}_x \rangle$) one can get by using SQM and DQM schemes in a 5-H spin cluster at an average distance from the NV sensor of $\approx 3.1 \text{ nm}$. The hyperfine vectors of the nuclear cluster are $\vec{A}_1 = (2\pi) \times [0.97, 3.18, -4.14]$, $\vec{A}_2 =$

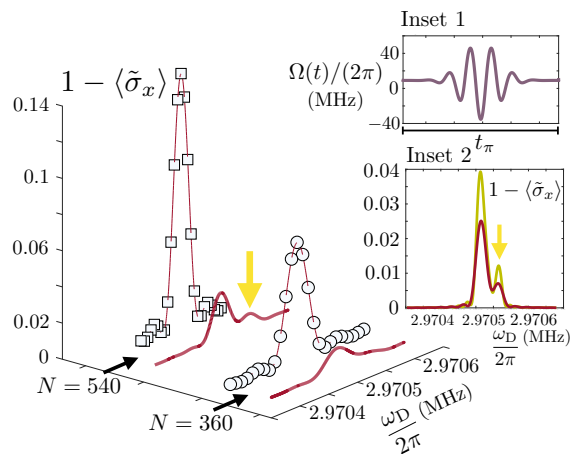


FIG. 2. Solid-red curves (wide curves) corresponds to ideal SQM schemes (i.e. these signals appear after the applying instantaneous π pulses). Thin-red lines are the signals appearing with DQM with instantaneous π pulses, while circles and squares have been obtained with the modulated $\Omega(t)$ in the Inset 1. Inset 2, emergence of a secondary peak. Note this does not occur in the case of our DQM schemes with tailored $\Omega(t)$.

$(2\pi) \times [-2.09, 2.69, 0.44]$, $\vec{A}_3 = (2\pi) \times [-1.84, 3.18, -0.13]$, $\vec{A}_4 = (2\pi) \times [-2.25, 3.42, -0.69]$, and $\vec{A}_5 = (2\pi) \times [-1.73, 3.00, -1.22]$ kHz. All signals in Fig. 2 have been computed at a large $B_z = 3$ T. The solid-red curves in Fig. 2 correspond to signals obtained with SQM protocols that employ instantaneous π pulses (i.e. non-realistic) ordered as $(XYXYXYX)^N$ for $N = 360, 540$. Note that for SQM, a single π pulse is enough to flip the σ_z operator in Eq. (8). Thin-red-lines and overlapping circles and squares in Fig. 2 are the obtained signals for DQM schemes. In particular, thin-red-lines assume instantaneous π pulses following the ordering in Fig. 1 (b), while the overlapping circles and squares are obtained with our method involving a tailored $\Omega(t)$ that is shown in the Inset 1 (for the plot we repeated a number $N = 360, 540$ the ideal sequence made of instantaneous pulses, and the realistic sequence with finite-width pulses). We stress that, this $\Omega(t)$ has been used to generate each π pulse in the three-pulse-sequences $\tilde{U}_{[\pi,0]}^{[+1,-1,+1]}$ and $\tilde{U}_{[\pi,\pi/2]}^{[-1,+1,-1]}$. Furthermore, as it can be clearly appreciated in Inset 1, the maximum value for the tailored Rabi frequency is $\approx (2\pi) \times 40$ MHz while $t_\pi \approx 0.16$ μ s. Then, even under the latter conditions of moderate MW power and long π pulses that extend over several Larmor periods (recall that, for H nuclei at $B_z = 3$ T one Larmor period is ≈ 7.8 ns) we reproduce the signal corresponding to an ideal DQM scheme using instantaneous π pulses (i.e. with infinite MW power). In addition, the simulations leading to circles and squares in Fig. 2 have been performed by considering an error of 1% in the MW field drivings, as well as an energy shift of $(2\pi) \times 20$ kHz on the NV spin transitions $|0\rangle \leftrightarrow |\pm 1\rangle$. In these conditions we observe no deviation with respect to the ideal

case of instantaneous π pulses (thin-red-lines) which certifies the robustness of our method.

Now we can better analyse the benefits of our method in nanoscale NMR. Firstly, in Fig. 2, it gets clear that with DQM schemes we obtain signals with a larger contrast than those obtained with SQM protocols. Secondly, the effect of the inhomogeneous broadening in SQM can be already appreciated in Fig. 2 with the emergence of a secondary peak (marked with a yellow arrow) in the case of $N = 540$. To better visualise it, in the Inset 2 we have plotted the SQM signals for $N = 540$ (solid-red) and for $N = 720$ (clear-green). Here it can be clearly seen the secondary peak that appears as a result of the magnetic field gradient ($\frac{1}{2} \sum_j \vec{A}_j \cdot \vec{I}_j$) introduced by SQM protocols. It is important to remark that these unwanted resonances induce ambiguities in the physical interpretation of the spectrum, since any secondary peak can be understood as arising from, e.g., a chemical shift that deviates the resonance frequencies of the nuclei in the sample. On the contrary, as it is demonstrated in Fig. 2, our DQM schemes produce clear peaks at the natural resonance frequency of the nuclei (i.e. when $43\omega_D = \omega_L$) which confirms that our method does not contaminate the nuclear cluster with magnetic field gradients. Finally, owing to the introduced design for $\Omega(t)$, our DQM methods can operate in the regime of large B_z fields where chemical shifts get enhanced⁴².

IV. CONCLUSIONS

We presented a method for DQM at large static magnetic fields. This is a regime where important parameters, such as the chemical shift that encodes structural information, get enhanced. Via the introduction of appropriately tuned $\Omega(t)$ we get larger contrasts in the nanoscale NMR signal. In addition, our method avoids spectral broadenings induced by the magnetic field gradients that appear in commonly used SQM protocols. This is of special importance for the measurements of natural frequency deviations in the nuclear spins of the sample. Our method is general, since it can be adapted to any DD sequence while it is applicable in different quantum sensors.

ACKNOWLEDGMENTS

Authors acknowledge financial support from Spanish Government PGC2018-095113-B-I00 (MCIU/AEI/FEDER, UE), Basque Government IT986-16, as well as from QMiCS (820505) and OpenSuperQ (820363) of the EU Flagship on Quantum Technologies, and to the EU FET Open Grant Quromorphic (828826). J.C. acknowledges support by the Juan de la Cierva grant IJCI-2016-29681, and to the UPV/EHU grant EHUroPE. I. A. acknowledges support to the Basque Government PhD grant PRE-2015-1-0394.

¹ C. L. Degen, F. Reinhard, and P. Cappellaro, Rev. Mod. Phys. **89**, 035002 (2017).

² M. W. Doherty, N. B. Manson, P. Delaney, F. Jelezko, J. Wrachtrup, and L. C. L. Hollenberg, Phys. Rep. **528**, 1 (2013).

- ³ V. V. Dobrovitski, G. D. Fuchs, A. L. Falk, C. Santori, and D.D. Awschalom, *Annu. Rev. Condens. Matter Phys.* **4**, 23 (2013).
- ⁴ L. Rondin, J. P. Tetienne, T. Hingant, J. F. Roch, P. Maletinsky, and V. Jacques, *Rep. Prog. Phys.* **77**, 056503 (2014).
- ⁵ R. Schirhagl, K. Chang, M. Loretz, and C. L. Degen. *Annu. Rev. Phys. Chem.* **65**, 83 (2014).
- ⁶ Y. Wu, F. Jelezko, M. B. Plenio, and T. Weil, *Angew. Chem.* **55**, 6586 (2016).
- ⁷ A. M. Souza, G. A. Álvarez, and D. Suter, *Phil. Trans. R. Soc. A* **370**, 4748 (2012).
- ⁸ S. R. Hartmann and E. L. Hahn, *Phys. Rev.* **128**, 2042 (1962).
- ⁹ A. A. Maudsley, *J. Magn. Reson.* **69**, 488 (1986).
- ¹⁰ T. Gullion, D. B. Baker, and M. S. Conradi, *J. Magn. Reson.* **89**, 479 (1990).
- ¹¹ A. M. Souza, G. A. Álvarez, and D. Suter, *Phys. Rev. Lett.* **106**, 240501 (2011).
- ¹² J. Casanova, Z.-Y. Wang, J. F. Haase, and M. B. Plenio, *Phys. Rev. A* **92**, 042304 (2015).
- ¹³ Z.-Y. Wang, J. Casanova, and M. B. Plenio, *Nat. Commun.* **8**, 14660 (2017).
- ¹⁴ J. E. Lang, J. Casanova, Z.-Y. Wang, M. B. Plenio, and T. S. Monteiro, *Phys. Rev. Applied* **7**, 054009 (2017).
- ¹⁵ I. Arrazola, J. Casanova, J. S. Pedernales, Z.-Y. Wang, E. Solano, and M. B. Plenio, *Phys. Rev. A* **97**, 052312 (2018).
- ¹⁶ J. M. Taylor, P. Cappellaro, L. Childress, L. Jiang, D. Budker, P. R. Hemmer, A. Yacoby, R. Walsworth, and M. D. Lukin, *Nat. Phys.* **4**, 810 (2008).
- ¹⁷ S. Kolkowitz, Q. P. Unterreithmeier, S. D. Bennett, and M. D. Lukin, *Phys. Rev. Lett.* **109**, 137601 (2012).
- ¹⁸ T. H. Taminiau, J. J. T. Wagenaar, T. van der Sar, F. Jelezko, V. V. Dobrovitski, and R. Hanson, *Phys. Rev. Lett.* **109**, 137602 (2012).
- ¹⁹ N. Zhao, J. Honert, B. Schmid, M. Klas, J. Isoya, M. Markham, D. Twitchen, F. Jelezko, R.-B. Liu, H. Fedder, and J. Wrachtrup, *Nat. Nanotech.* **7**, 657 (2012).
- ²⁰ P. London, J. Scheuer, J.-M. Cai, I. Schwarz, A. Retzker, M. B. Plenio, M. Katagiri, T. Teraji, S. Koizumi, J. Isoya, R. Fischer, L. P. McGuinness, B. Naydenov, and F. Jelezko, *Phys. Rev. Lett.* **111**, 067601 (2013).
- ²¹ J. Zopes, K. Herb, K. S. Cujia, and C. L. Degen, *Phys. Rev. Lett.* **121**, 170801 (2018).
- ²² J. Zopes, K. S. Cujia, K. Sasaki, J. M. Boss, K. M. Itoh, and C. L. Degen, *Nat. Commun.* **9**, 4678 (2018).
- ²³ C. E. Bradley, J. Randall, M. H. Abobeih, R. C. Berrevoets, M. J. Degen, M. A. Bakker, M. Markham, D. J. Twitchen, and T. H. Taminiau, *Phys. Rev. X* **9**, 031045 (2019).
- ²⁴ M. H. Abobeih, J. Randall, C. E. Bradley, H. P. Bartling, M. A. Bakker, M. J. Degen, M. Markham, D. J. Twitchen, and T. H. Taminiau, *Nature* **576**, 411 (2019).
- ²⁵ H. J. Mamin, M. Kim, M. H. Sherwood, C. T. Rettner, K. Ohno, D. D. Awschalom, and D. Rugar, *Science* **339**, 557 (2013).
- ²⁶ T. Staudacher, F. Shi, S. Pezzagna, J. Meijer, J. Du, C. A. Meriles, F. Reinhard, and J. Wrachtrup, *Science* **339**, 561 (2013).
- ²⁷ C. Müller, X. Kong, J.-M. Cai, K. Melentijević, A. Stacey, M. Markham, D. Twitchen, J. Isoya, S. Pezzagna, J. Meijer, J. F. Du, M. B. Plenio, B. Naydenov, L. P. McGuinness, and F. Jelezko, *Nat. Commun.* **5**, 4703 (2014).
- ²⁸ F. Shi, Q. Zhang, P. Wang, H. Sun, J. Wang, X. Rong, M. Chen, C. Ju, F. Reinhard, H. Chen, J. Wrachtrup, J. Wang, and J. Du, *Science* **347**, 1135 (2015).
- ²⁹ I. Lovchinsky, A. O. Sushkov, E. Urbach, N. P. de Leon, S. Choi, K. De Greve, R. Evans, R. Gertner, E. Bersin, C. Müller, L. McGuinness, F. Jelezko, R. L. Walsworth, H. Park, and M. D. Lukin, *Science* **351**, 836 (2016).
- ³⁰ N. Aslam, M. Pfender, P. Neumann, R. Reuter, A. Zappe, F. F. de Oliveira, A. Denisenko, H. Sumiya, S. Onoda, J. Isoya, and J. Wrachtrup, *Science* **357**, 67 (2017).
- ³¹ S. J. DeVience, L. M. Pham, I. Lovchinsky, A. O. Sushkov, N. Bar-Gill, C. Belthangady, F. Casola, M. Corbett, H. Zhang, M. Lukin, H. Park, A. Yacoby, and R. L. Walsworth, *Nat. Nanotech.* **10**, 129 (2015).
- ³² D. R. Glenn, D. B. Bucher, J. Lee, M. D. Lukin, H. Park, and R. L. Walsworth, *Nature* **555**, 351 (2018).
- ³³ T. Roskopf, J. Zopes, J. M. Boss, and C. L. Degen, *npj Quantum Information* **3**, 33 (2017).
- ³⁴ S. Schmitt, T. Gefen, F. M. Stürner, T. Uden, G. Wolff, C. Müller, J. Scheuer, B. Naydenov, M. Markham, S. Pezzagna, J. Meijer, I. Schwarz, M. Plenio, A. Retzker, L. P. McGuinness, and F. Jelezko, *Science* **356**, 832 (2017).
- ³⁵ J. M. Boss, K. S. Cujia, J. Zopes, C. L. Degen, *Science* **356**, 837 (2017).
- ³⁶ F. Reinhard, F. Shi, N. Zhao, F. Rempp, B. Naydenov, J. Meijer, L. T. Hall, L. Hollenberg, J. Du, R.-B. Liu, and J. Wrachtrup, *Phys. Rev. Lett.* **108**, 200402 (2012).
- ³⁷ K. Fang, V. M. Acosta, C. Santori, Z. Huang, K. M. Itoh, H. Watanabe, S. Shikata, and R. G. Beausoleil, *Phys. Rev. Lett.* **110**, 130802 (2013).
- ³⁸ H. J. Mamin, M. H. Sherwood, M. Kim, C. T. Rettner, K. Ohno, D. D. Awschalom, and D. Rugar, *Phys. Rev. Lett.* **113**, 030803 (2014).
- ³⁹ J. Casanova, Z.-Y. Wang, I. Schwartz, and M. B. Plenio, *Phys. Rev. Applied* **10**, 044072 (2018).
- ⁴⁰ J. Casanova, E. Torrontegui, M. B. Plenio, J. J. García-Ripoll, and E. Solano, *Phys. Rev. Lett.* **122**, 010407 (2019).
- ⁴¹ I. Arrazola, E. Solano, and J. Casanova, *Phys. Rev. B* **99**, 245405 (2019).
- ⁴² M. H. Levitt, *Spin Dynamics: Basics of Nuclear Magnetic Resonance* (Wiley, West Sussex, 2008).
- ⁴³ E. C. Reynhardt and G. L. High, *Prog. Nucl. Magn. Reson. Spectrosc.* **38**, 37 (2001).
- ⁴⁴ See Supplemental Material for further details.
- ⁴⁵ P. Allard and T. Härd, *Journal of Magnetic Resonance* **153**, 15 (2001).
- ⁴⁶ J. R. Maze, J. M. Taylor, and M. D. Lukin, *Phys. Rev. B* **78**, 094303 (2008).
- ⁴⁷ J. Casanova, Z.-Y. Wang, and M. B. Plenio, *Phys. Rev. A* **96**, 032314 (2017).

Supplemental Material: Double Quantum Magnetometry at Large Static Magnetic Fields

CONTENTS

I. Three-Pulse-sequences	1
A. First three-pulse-sequence $\tilde{U}_{[\pi,0]}^{[+1,-1,+1]}$	1
1. First pulse	1
2. Second pulse	2
3. Third pulse	2
B. Second three-pulse-sequence $\tilde{U}_{[\pi,\pi/2]}^{[-1,+1,-1]}$	2
1. First pulse	3
2. Second pulse	3
3. Third pulse	3
II. Calculating the f_l coefficient for top-hat pulses	3
III. Theoretically expected signal	4
IV. Finding appropriate $\Omega(t)$ functions	4
References	5

I. THREE-PULSE-SEQUENCES

Here, we show in detail the achievement of the modulation function of the S_z operator involved in the three-pulse-sequences $\tilde{U}_{[\pi,0]}^{[+1,-1,+1]}$ and $\tilde{U}_{[\pi,\pi/2]}^{[-1,+1,-1]}$.

A. First three-pulse-sequence $\tilde{U}_{[\pi,0]}^{[+1,-1,+1]}$

One can demonstrate that a 2ϕ pulse of the kind $\exp[\pm i\phi(e^{-i\varphi}|\pm 1\rangle\langle 0| + e^{i\varphi}|0\rangle\langle \pm 1|)]$ on the $S = 1$ manifold of the NV center is

$$U_{[\pm 2\phi, \varphi]}^{\pm 1} = \exp[\pm i\phi(e^{-i\varphi}|\pm 1\rangle\langle 0| + e^{i\varphi}|0\rangle\langle \pm 1|)] \\ = I + (\cos \phi - 1)(|\pm 1\rangle\langle \pm 1| + |0\rangle\langle 0|) \pm i \sin \phi (e^{-i\varphi}|\pm 1\rangle\langle 0| + e^{i\varphi}|0\rangle\langle \pm 1|), \quad (\text{S1})$$

where $I = |1\rangle\langle 1| + |0\rangle\langle 0| + |-1\rangle\langle -1|$.

1. First pulse

In this manner, the application of a 2ϕ pulse over the X axis (i.e. $\varphi = 0$) and acting, e.g., on the $\{|1\rangle, |0\rangle\}$ spin manifold transforms the S_z operator as

$$\exp[+i\phi(|1\rangle\langle 0| + |0\rangle\langle 1|)]S_z \exp[-i\phi(|1\rangle\langle 0| + |0\rangle\langle 1|)] = \\ \cos \phi^2 |1\rangle\langle 1| + \sin \phi^2 |0\rangle\langle 0| - |-1\rangle\langle -1| - i \cos \phi \sin \phi (|1\rangle\langle 0| - |0\rangle\langle 1|). \quad (\text{S2})$$

The basis of an $S = 1$ Hilbert space has a dimension $d = 9$. Then, by using a similar basis (note we restrict to only the diagonal terms) for $S = 1$ than the one proposed one in^{S1} we get

$$|1\rangle\langle 1| = \frac{1}{3}I + \frac{1}{2}S_z + \frac{1}{6}G, \\ |0\rangle\langle 0| = \frac{1}{3}I - \frac{1}{3}G, \\ |-1\rangle\langle -1| = \frac{1}{3}I - \frac{1}{2}S_z + \frac{1}{6}G, \quad (\text{S3})$$

where

$$\begin{aligned} I &= |1\rangle\langle 1| + |0\rangle\langle 0| + |-1\rangle\langle -1|, \\ S_z &= |1\rangle\langle 1| - |-1\rangle\langle -1|, \\ G &= |1\rangle\langle 1| - 2|0\rangle\langle 0| + |-1\rangle\langle -1|. \end{aligned} \quad (\text{S4})$$

For a final $\phi = \pi/2$ (i.e. we applied the $U_{[\pi,0]}^{+1}$ operator, this is a π pulse over the X axis in the $\{|1\rangle, |0\rangle\}$ spin manifold) S_z transforms to $|0\rangle\langle 0| - |-1\rangle\langle -1|$, while during the application of the X pulse S_z evolves as $\frac{1}{2}(\cos^2 \phi + 1)$.

Then, during this first pulse we have that S_z transforms as

$$S_z \longrightarrow \frac{1}{2}(\cos^2 \phi + 1) S_z - \frac{1}{2}(\sin^2 \phi) G. \quad (\text{S5})$$

While for the final value of $\phi = \pi/2$ we find that S_z has changed as $S_z \longrightarrow \frac{1}{2} S_z - \frac{1}{2} G = |0\rangle\langle 0| - |-1\rangle\langle -1|$.

2. Second pulse

The next step is to interchange the $|0\rangle$ and $|-1\rangle$ spin components. This is achieved by applying the $U_{\pm 2\phi,0}^{-1,0}$ pulse operator for a final value of $\phi = \pi/2$. More specifically, this is

$$U_{2\phi,0}^{-1,0}(|0\rangle\langle 0| - |-1\rangle\langle -1|)U_{-2\phi,0}^{-1,0} = (\cos^2 \phi - \sin^2 \phi)(|0\rangle\langle 0| - |-1\rangle\langle -1|) - 2i \sin \phi \cos \phi (|0\rangle\langle -1| - |-1\rangle\langle 0|). \quad (\text{S6})$$

Then, by using again the transformation in Eq. (S3) one can find

$$\frac{1}{2} S_z - \frac{1}{2} G = |0\rangle\langle 0| - |-1\rangle\langle -1| \longrightarrow \frac{1}{2}(\cos^2 \phi - \sin^2 \phi)(S_z - G_z). \quad (\text{S7})$$

Again, for the final value of $\phi = \pi/2$ the final state is $\frac{1}{2}(G_z - S_z) = -(|0\rangle\langle 0| - |-1\rangle\langle -1|)$

3. Third pulse

Finally, we apply a last pulse defined by $U_{2\phi,0}^{1,0}$. This is

$$\begin{aligned} U_{2\phi,0}^{1,0}(-|0\rangle\langle 0| + |-1\rangle\langle -1|)U_{-2\phi,0}^{1,0} = \\ -\cos^2 \phi |0\rangle\langle 0| - \sin^2 \phi |1\rangle\langle 1| + |-1\rangle\langle -1| + i \cos \phi \sin \phi (|0\rangle\langle 1| - |1\rangle\langle 0|). \end{aligned} \quad (\text{S8})$$

This implies that, during this last pulse, the $\frac{1}{2}(G_z - S_z) = -(|0\rangle\langle 0| - |-1\rangle\langle -1|)$ operator changes as

$$\frac{1}{2}(G_z - S_z) = -(|0\rangle\langle 0| - |-1\rangle\langle -1|) \longrightarrow -\frac{1}{2}[1 + \sin^2 \phi]S_z + \frac{1}{2}\cos^2 \phi G \quad (\text{S9})$$

Summarising, the evolution of the S_z operator during each step of the three-pulse-sequence $\tilde{U}_{[\pi,0]}^{[+1,-1,+1]} = U_{[\pi,0]}^{+1} U_{[\pi,0]}^{-1} U_{[\pi,0]}^{+1}$ is

$$\begin{aligned} \text{First pulse : } & \frac{1}{2}(\cos^2 \phi + 1) S_z - \frac{1}{2}(\sin^2 \phi) G \\ \text{Second pulse : } & \frac{1}{2}(\cos^2 \phi - \sin^2 \phi)(S_z - G_z) \\ \text{Third pulse : } & -\frac{1}{2}[1 + \sin^2 \phi]S_z + \frac{1}{2}\cos^2 \phi G \end{aligned} \quad (\text{S10})$$

B. Second three-pulse-sequence $\tilde{U}_{[\pi,\pi/2]}^{[-1,+1,-1]}$

Here we will study the second three-pulse-sequence $\tilde{U}_{[\pi,\pi/2]}^{[-1,+1,-1]}$ that would complete one period of the S_z operator.

1. First pulse

We apply the $U_{[\phi,\pi/2]}^{-1}$ pulse to the $-S_z$ operator (note this is the operator we get after using the previously explained $\tilde{U}_{[\pi,0]}^{[+1,-1,+1]}$ on the initial S_z) and find

$$\exp[+i\phi(e^{-i\frac{\pi}{2}}| - 1\rangle\langle 0| + e^{i\frac{\pi}{2}}|0\rangle\langle -1|)](-S_z)\exp[-i\phi(e^{-i\frac{\pi}{2}}| - 1\rangle\langle 0| + e^{i\frac{\pi}{2}}|0\rangle\langle -1|)] = \cos^2\phi| - 1\rangle\langle -1| + \sin^2\phi|0\rangle\langle 0| - |1\rangle\langle 1| - i\cos\phi\sin\phi(e^{-i\frac{\pi}{2}}| - 1\rangle\langle 0| - e^{i\frac{\pi}{2}}|0\rangle\langle -1|). \quad (\text{S11})$$

Then, we have that $-S_z$ changes as

$$-S_z \longrightarrow -\frac{1}{2}(\cos^2\phi + 1)S_z - \frac{1}{2}(\sin^2\phi)G. \quad (\text{S12})$$

For the final value of $\phi = \frac{\pi}{2}$ we have $-S_z \longrightarrow -\frac{1}{2}(S_z + G) = -(|1\rangle\langle 1| - |0\rangle\langle 0|)$

2. Second pulse

Now we apply the $U_{[\phi,\pi/2]}^{+1}$ pulse and get

$$\exp[+i\phi(e^{-i\frac{\pi}{2}}|1\rangle\langle 0| + e^{i\frac{\pi}{2}}|0\rangle\langle 1|)](|0\rangle\langle 0| - |1\rangle\langle 1|)\exp[-i\phi(e^{-i\frac{\pi}{2}}|1\rangle\langle 0| + e^{i\frac{\pi}{2}}|0\rangle\langle 1|)] = (\cos^2\phi - \sin^2\phi)(|0\rangle\langle 0| - |1\rangle\langle 1|) - 2i\cos\phi\sin\phi(e^{i\frac{\pi}{2}}|0\rangle\langle 1| - e^{-i\frac{\pi}{2}}|1\rangle\langle 0|). \quad (\text{S13})$$

Then, we have the following transformation

$$-\frac{1}{2}(S_z + G) \longrightarrow -\frac{1}{2}(\cos^2\phi - \sin^2\phi)(S_z + G), \quad (\text{S14})$$

while for the final value of $\phi = \pi/2$ we have $-\frac{1}{2}(S_z + G) = (|1\rangle\langle 1| - |0\rangle\langle 0|)$

3. Third pulse

We finally use the $U_{[\phi,\pi/2]}^{-1}$ pulse to complete the sequence. This leads to

$$\exp[+i\phi(e^{-i\frac{\pi}{2}}| - 1\rangle\langle 0| + e^{i\frac{\pi}{2}}|0\rangle\langle -1|)](|1\rangle\langle 1| - |0\rangle\langle 0|)\exp[-i\phi(e^{-i\frac{\pi}{2}}| - 1\rangle\langle 0| + e^{i\frac{\pi}{2}}|0\rangle\langle -1|)] = -\cos^2\phi|0\rangle\langle 0| - \sin^2\phi| - 1\rangle\langle -1| + |1\rangle\langle 1| - i\cos\phi\sin\phi(e^{-i\frac{\pi}{2}}| - 1\rangle\langle 0| - e^{i\frac{\pi}{2}}|0\rangle\langle -1|). \quad (\text{S15})$$

Then, we have the transformation

$$-\frac{1}{2}(S_z + G) = (|1\rangle\langle 1| - |0\rangle\langle 0|) = \frac{1}{2}[1 + \sin^2\phi]S_z + \frac{1}{2}\cos^2\phi G. \quad (\text{S16})$$

Then, for a final value $\phi = \pi/2$ we recover the S_z operator.

Summarising, the evolution of the $-S_z$ operator during the three-pulse-sequence $\tilde{U}_{[\pi,\pi/2]}^{[-1,+1,-1]}$ is

$$\begin{aligned} \text{First pulse : } & -\frac{1}{2}(\cos^2\phi + 1)S_z - \frac{1}{2}(\sin^2\phi)G \\ \text{Second pulse : } & -\frac{1}{2}(\cos^2\phi - \sin^2\phi)(S_z + G) \\ \text{Third pulse : } & +\frac{1}{2}[1 + \sin^2\phi]S_z + \frac{1}{2}\cos^2\phi G \end{aligned} \quad (\text{S17})$$

II. CALCULATING THE f_i COEFFICIENT FOR TOP-HAT PULSES

After the application of the following sequence to the S_z operator

$$\left(- \quad - \quad - \quad \tilde{U}_{[\pi,\pi/2]}^{[-1,+1,-1]} \quad - \quad - \quad - \quad - \quad - \quad \tilde{U}_{[\pi,0]}^{[+1,-1,+1]} \quad - \quad - \quad - \right), \quad (\text{S18})$$

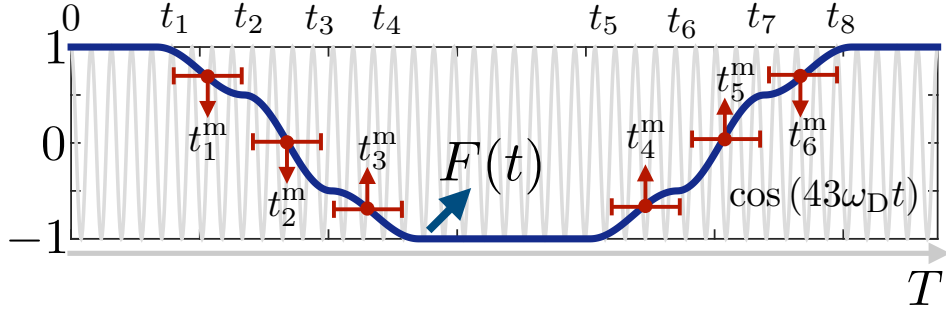


FIG. S1. Modulation function $F(t)$ (solid-blue) appearing after the application of the sequence in Eq. (S18). For this plot, we have selected the 43th harmonic as the target harmonic (see figure background in clear grey) since this is the one we use for the numerical simulations in the main text. For the sake of simplicity we assume $(t_2 - t_1) = (t_3 - t_2) = (t_4 - t_3) = (t_6 - t_5) = (t_7 - t_6) = (t_8 - t_7) = t_\pi$. In addition, in this plot it is marked the central point of each time interval where a π pulse is displayed. This is, e.g., the first top-hat π pulse is displayed in the interval $(t_2 - t_1)$ being t_1^m its center.

note that with the symbol “— — —” we indicate the free evolution of the S_z operator, one would get the modulation function $F(t)$ that appears in Fig. S1. Also, we want to remark that the sequence in Eq. (S18) appears when the top-hat pulses in Fig. 1 (a) of the main text is displayed.

Then, taking into account the expressions for $F(t)$ calculated in the previous section and that we defined $t_\pi = \frac{2\pi r}{\omega_L}$, one can easily find that

$$f_{43} = \frac{2}{T} \int_0^T F(s) \cos(43\omega_D s) ds = \frac{36 \cos^3(\pi r)}{\pi 43(-9 + 36r^2)}, \quad (\text{S19})$$

or, in general

$$f_l = \frac{2}{T} \int_0^T F(s) \cos(l\omega_D s) ds = \frac{(-1)^{\frac{l+1}{2}} 36 \cos^3(\pi r)}{\pi l(-9 + 36r^2)}. \quad (\text{S20})$$

III. THEORETICALLY EXPECTED SIGNAL

For the resonant Hamiltonian $H = \frac{f_{43}}{2} S_z A^x I_x$ proposed in the main text, one can easily calculate that, for an initial state NV-nucleus state $\rho_0 = \frac{1}{2}(|1\rangle + |-1\rangle)(\langle 1| + \langle -1|) \otimes \frac{1}{2}I$ (i.e. the initial NV state is the superposition $\frac{1}{\sqrt{2}}(|1\rangle + |-1\rangle)$, and the nucleus in a thermal state that we approximate to $\frac{1}{2}I_{2 \times 2}$) the theoretically expected signal is

$$\langle \tilde{\sigma}_x \rangle = \text{Tr} \left(e^{-i \frac{f_{43}}{2} S_z A^x I_x t} \rho_0 e^{i \frac{f_{43}}{2} S_z A^x I_x t} \tilde{\sigma}_x \right) = \cos \left(\frac{f_{43}}{2} A^x t \right). \quad (\text{S21})$$

IV. FINDING APPROPRIATE $\Omega(t)$ FUNCTIONS

The shape of the $F(t)$ function that appears after the application of top-hat pulses can be seen in Fig. S1 and, as we have demonstrated in Sec. II, it leads to a decreasing value for the f_l coefficients.

As we are introducing three π pulses per flip of the S_z operator, i.e. we need three π pulses to generate the propagators $\tilde{U}_{[\pi,0]}^{[+1,-1,+1]}$ and $\tilde{U}_{[\pi,\pi/2]}^{[-1,+1,-1]}$ we can always write a f_l coefficient as (see Fig. S1)

$$\begin{aligned} f_l = & \frac{2}{T} \left[\int_0^{t_1} \cos(l\omega_D s) ds + \int_{t_1}^{t_2} F(s) \cos(l\omega_D s) ds + \int_{t_2}^{t_3} F(s) \cos(l\omega_D s) ds + \int_{t_3}^{t_4} F(s) \cos(l\omega_D s) ds \right. \\ & - \int_{t_4}^{t_5} \cos(l\omega_D s) ds + \int_{t_5}^{t_6} F(s) \cos(l\omega_D s) ds + \int_{t_6}^{t_7} F(s) \cos(l\omega_D s) ds + \int_{t_7}^{t_8} F(s) \cos(l\omega_D s) ds \\ & \left. + \int_{t_8}^T \cos(l\omega_D s) ds \right]. \quad (\text{S22}) \end{aligned}$$

Then, if we find a $F(t)$ function such that it cancels the integral during the π pulses, the above equation reduces to

$$f_i = \frac{2}{T} \left[\int_0^{t_1} \cos(l\omega_D s) ds - \int_{t_4}^{t_5} \cos(l\omega_D s) ds + \int_{t_8}^T \cos(l\omega_D s) ds \right]. \quad (\text{S23})$$

Now, as it is standard in dynamical decoupling techniques we select $(t_1 - 0) = \frac{1}{2}(t_5 - t_4) = \frac{1}{2}(T - t_8)$. In addition, we assume that each π pulse has the same duration, this is $(t_2 - t_1) = (t_3 - t_2) = (t_4 - t_3) = (t_6 - t_5) = (t_7 - t_6) = (t_8 - t_7) = t_\pi$, then it can be calculated that Eq. (S23) reads

$$f_i = \frac{4}{\pi l} \cos\left(\pi \frac{3t_\pi}{T/l}\right) \sin(\pi l/2), \quad (\text{S24})$$

which takes the maximum value $|f_i| = \frac{4}{\pi l}$ (this is the value we target for our numerical simulations in the main text) when each modulated π pulse takes an extension determined by

$$t_\pi = \frac{n}{3} T/l, \quad (\text{S25})$$

with n being a natural number.

Now, we have to find a form for $F(t)$ such that it eliminates the integrals involving π pulses in Eq. (S22). Our solution correspond to introduce a $F(t)$ with two components. The first component is the shape that $F(t)$ acquires in case of applying only top-hat π pulses, the second one is an oscillating function such that it cancels the area of the first component.

In particular, for the first π pulse we propose that $F(t)$ takes the following form

$$F(t) = \frac{1}{2} \left[\cos^2\left(\frac{\pi(t-t_1)}{t_\pi}\right) + 1 \right] - \alpha_1 \cos\left(\frac{2\pi k}{T} t\right) \exp[-(t-t_1^m)^2/(2\sigma_1^2)], \quad (\text{S26})$$

with $t \in [t_2, t_1]$, t_1^m the central point of the interval $[t_2, t_1]$ and σ_1 the width (that one can freely adjust) of the Gaussian function in the second component of Eq. (S26). Note that, as we have explained, the first component of Eq. (S26) is $\frac{1}{2} \left[\cos^2\left(\frac{\pi(t-t_1)}{t_\pi}\right) + 1 \right]$, which is the aspect of $F(t)$ during a top-hat π pulse, see Eq (S5).

Then the only missing parameter is the constant α_1 that we will use to cancel the integral $\int_{t_1}^{t_2} F(s) \cos(l\omega_D s) ds$, see Eq. (S22). In this manner, the value of α_1 is

$$\alpha_1 = - \frac{\int_{t_1}^{t_2} \frac{1}{2} \left[\cos^2\left(\frac{\pi(s-t_1)}{t_\pi}\right) + 1 \right] \cos(l\omega_D s) ds}{\int_{t_1}^{t_2} \cos\left(\frac{2\pi k}{T} t\right) \exp[-(t-t_1^m)^2/(2\sigma_1^2)] \cos(l\omega_D s) ds} \quad (\text{S27})$$

Finally, once all parameters are selected we can find the value of the Rabi frequency that generates the $F(t)$ in Eq. (S26) as

$$\Omega(t) = \frac{\partial}{\partial t} \arccos[F(t)]. \quad (\text{S28})$$

The previous equation can be understand by noting that the effect of the first driving $H = \frac{\Omega(t)}{2}(e^{-i\varphi}|+1\rangle\langle 0| + e^{i\varphi}|0\rangle\langle +1|)$ that acts over the $|0\rangle \leftrightarrow |+1\rangle$ NV spin transition, is

$$S_z \longrightarrow \frac{1}{2} \left(\cos^2 \int_{t_1}^t \frac{\Omega(s)}{2} ds + 1 \right) S_z - \frac{1}{2} (\sin^2 \phi) G. \quad (\text{S29})$$

Then, one only has to invert the equation

$$F(t) = \frac{1}{2} \left(\cos^2 \int_{t_1}^t \frac{\Omega(s)}{2} ds + 1 \right), \quad (\text{S30})$$

to find $\Omega(t)$. If we do that, we get the modulated $\Omega(t)$ that appears in Fig. 2 of the main text.

The same strategy has to be applied to eliminate the integrals of all π pulses in Eq. (S23). Note that for each case (i.e. for each π pulse leading to the three-pulse-sequences) the first component of $F(t)$ has a different aspect, but fortunately we have calculated all of them in Sec. I of this Supplemental Material.